The Astrophysical Journal, 966:147 (14pp), 2024 May 10 https://doi.org/10.3847/1538-4357/ad3800
© 2024. The Author(s). Published by the American Astronomical Society.
OPEN ACCESS

Latest Evolution of the X-Ray Remnant of SN 1987A: Beyond the Inner Ring

Aravind P. Ravi[1,7], Sangwook Park[1], Svetozar A. Zhekov[2], Salvatore Orlando[3], Marco Miceli[3,4], Kari A. Frank[5], Patrick S. Broos[6], and David N. Burrows[6]
[1] Department of Physics, University of Texas at Arlington, Box 19059, Arlington, TX 76019, USA; apazhayathravi@ucdavis.edu
[2] Institute of Astronomy and National Astronomical Observatory (Bulgarian Academy of Sciences), 72 Tsarigradsko Chaussee Blvd., Sofia 1784, Bulgaria
[3] INAF-Osservatorio Astronomico di Palermo, Piazza del Parlamento 1, 90134 Palermo, Italy
[4] Dipartimento di Fisica e Chimica, Universita degli Studi di Palermo, Piazza del Parlamento 1, 90134 Palermo, Italy
[5] CIERA, Northwestern University, 1800 Sherman, 8007 Evanston, IL 60201, USA
[6] Department of Astronomy and Astrophysics, Pennsylvania State University, University Park, PA 16802, USA
Received 2023 December 18; revised 2024 March 11; accepted 2024 March 23; published 2024 May 2

Abstract

Based on our Chandra imaging-spectroscopic observations, we present the latest evolution of the X-ray remnant of SN 1987A. Recent changes in the electron temperatures and volume emission measures suggest that the blast wave in SN 1987A is moving out of the dense inner ring structure, also called the equatorial ring (ER). The 0.5–2.0 keV X-ray light curve shows a linearly declining trend (by ∼4.5% yr^{-1}) between 2016 and 2020 as the blast wave heats the hitherto unknown circumstellar medium (CSM) outside the ER. While the peak X-ray emission in the latest 0.3–8.0 keV image is still within the ER, the radial expansion rate in the 3.0–8.0 keV images suggests an increasing contribution of the X-ray emission from less dense CSM since 2012, at least partly from beyond the ER. It is remarkable that, since 2020, the declining soft X-ray flux has stabilized around $\sim 7 \times 10^{-12}$ erg s^{-1} cm^{-2}, which may signal a contribution from the reverse-shocked outer layers of ejecta as predicted by the three-dimensional magnetohydrodynamic models. In the latest ACIS spectrum of supernova remnant 1987A in 2022 we report a significant detection of the Fe K line at ∼6.7 keV, which may be due to changing thermal conditions of the X-ray emitting CSM and/or the onset of reverse shock interactions with the Fe ejecta.

Unified Astronomy Thesaurus concepts: Supernova remnants (1667); Core-collapse supernovae (304)

1. Introduction

SN 1987A is a core-collapse supernova (SN) discovered on 1987 February 24 in the Large Magellanic Cloud (LMC). It has been the nearest (distance ∼51 kpc) and hence the brightest observed SN since the historic Kepler's SN in 1604 CE (see Arnett et al. 1989; McCray 1993; McCray & Fransson 2016, for detailed reviews). Being the closest observed SN since the advent of modern telescopes, SN 1987A is a unique and crucial astrophysical laboratory to study the early makings of a supernova remnant (SNR) and a neutron star. Thus, SN 1987A has been observed and studied extensively across the entire electromagnetic spectrum for >30 yr after the explosion.

Early optical observations of SN 1987A with the Hubble Space Telescope (HST) revealed an unusual triple-ring structure, the dense circumstellar medium (CSM) that was created by stellar winds from the massive progenitor and then photoionized by UV flash from the explosion itself (Burrows et al. 1995). These three rings, a bright inner equatorial ring (ER) and two faint outer rings, together form an hourglass structure. The inner ER is within a larger H II region of lower density (Chevalier & Dwarkadas 1995). While the origin of these structures is still unclear, it is likely the result of an interaction between the fast-moving, low-density blue supergiant wind with the slower, high-density red supergiant wind from different stages of the progenitor's evolution history (Luo & McCray 1991; Wang & Mazzali 1992; Morris & Podsiadlowski 2007). The observed X-ray images show a simpler structure with the emission primarily from the shocked ER (Burrows et al. 2000). With the best available X-ray spatial and spectral resolutions, the Chandra X-ray Observatory (Chandra) has been crucial to study the photometric, morphological, and spectroscopic evolution of the X-ray remnant of SN 1987A (SNR 1987A, hereafter).

As part of our ongoing Chandra X-ray monitoring program, we have observed SNR 1987A roughly every 6 months for the past 22 yr (total of 47 observations as of 2023 April). We have presented previous results of our Chandra monitoring campaign of SNR 1987A in the literature (e.g., Burrows et al. 2000; Park et al. 2002, 2004, 2005, 2006, 2011; Zhekov et al. 2010; Helder et al. 2013; Frank et al. 2016).

Previous results showed that the X-ray emission from SNR 1987A has been dominated by shock interaction with the dense CSM of the ER. As the shock encountered the main body of the ER around 2004 (∼6200 days after the SN), the expansion rate of the X-ray emitting ring decreased significantly from ∼6000 to ∼1700 km s^{-1} (Racusin et al. 2009). Until 2015 (∼10,500 days after the SN), this expansion rate has stayed relatively constant at ∼1800 km s^{-1} (Frank et al. 2016). The expansion rate of the X-ray emitting ring provides crucial morphological information, which can only be resolved by Chandra at these wavelengths.

At the same time as the shock moved into the main body of the dense ER, a sharp upturn was observed in the measured soft X-ray flux in the 0.5–2.0 keV energy range (Park et al. 2004, 2005). The X-ray flux continued to increase between 2004 and 2012, suggesting continuous shock-CSM interactions (Park et al. 2005, 2011; Maggi et al. 2012; Helder et al. 2013). Between 2012 and 2015, the soft X-ray leveled off, hinting at

[7] Current Address: Department of Physics and Astronomy, University of California, 1 Shields Avenue, Davis, CA 95616-5270, USA

Original content from this work may be used under the terms of the Creative Commons Attribution 4.0 licence. Any further distribution of this work must maintain attribution to the author(s) and the title of the work, journal citation and DOI.

the start of a new evolutionary phase as the blast wave started to move out of the dense ER (Frank et al. 2016). The X-ray light curve is a powerful probe of the density of the shocked CSM when sampled as frequently as our Chandra monitoring program. Both the X-ray light curves and spatially resolved images have been instrumental ingredients for providing observational constraints for modeling the evolution of SN 1987A (Chevalier & Dwarkadas 1995; Borkowski et al. 1997; Zhekov et al. 2010; Dewey et al. 2012; Potter et al. 2014; Orlando et al. 2015, 2019, 2020).

Recent optical, infrared, and radio monitoring observations have suggested that the shock front in SNR 1987A moved out of the dense ER several years ago and is now interacting with the low-density CSM that was produced in the red supergiant phase of the progenitor (e.g., Fransson et al. 2015; Arendt et al. 2016; Cendes et al. 2018; Larsson et al. 2019; Arendt et al. 2020). Our recent deep Chandra gratings spectroscopic study (Ravi et al. 2021) showed evidence for increasing electron temperatures and decreasing volume emission measures between 2011 and 2018, consistent with expected X-ray emission from the newly shocked CSM.

As the blast wave moves outward, the reverse shock is expected to develop, enclosing the cold ejecta. Three-dimensional magnetohydrodynamic (MHD) simulation models predict that the interaction between the outer layers of the ejecta and the reverse shock would become significant $\gtrsim$35 yr after the SN (i.e., $\gtrsim$2022 Orlando et al. 2015, 2020). In this period, as the blast wave leaves the ER, X-ray emission from the dense ER will fade, while that from the reverse-shocked ejecta will strengthen over time.

In this paper, we present our latest measurements of X-ray fluxes and the updated Chandra X-ray light curves as well as radial expansion measurements and morphological development of SNR 1987A, covering up to 2023 April (through $\sim$13,200 days after the SN). In Section 2, we describe our observations and methods of data reduction. In Section 3, we present X-ray light curves, radial expansion rates, and temporal evolution of the soft X-ray spectrum, including the development of the Fe K line flux. In Section 4, we discuss physical interpretations of our results, and we summarize them in Section 5.

2. Observations and Data Reduction

The 47 Chandra observations used in this work are presented in Table 1. Results from our Chandra monitoring observations between 1999 and 2015 have been previously discussed in the literature (Burrows et al. 2000; Park et al. 2002, 2004, 2005, 2006; Racusin et al. 2009; Park et al. 2011; Helder et al. 2013; Frank et al. 2016). Since 2016, there have been 15 new observations as part of our monitoring campaign (eight ACIS-S/HETG and seven HRC-S/LETG observations). Our Chandra monitoring observation taken in 2022 September (ObsID 27443 with the HRC-S/LETG configuration) was performed with a significantly shorter exposure time (13 ks) than our scheduled duration (59 ks) due to an unexpected anomaly that occurred in the detector. Thus, the utility of this observation was limited, and we did not include this data set in our analysis.

As discussed in Frank et al. (2016) and Helder et al. (2013), the ACIS observing configurations have been changed multiple times since 2008 to mitigate the photon pileup effects due to the very high count rates from the brightening SNR. Since 2008, HETG has been inserted to further reduce the pileup effects of the ACIS detector. In the epochs of 2008 July and 2009 January, we observed SNR 1987A both with and without HETG for calibration purposes to ensure a smooth transition between the two configurations (Frank et al. 2016). For these epochs, we use the bare ACIS data for imaging due to better count statistics. For spectral analysis at these epochs, we use the HETG observations, as the use of the grating reduces pileup in the observed CCD spectrum. Additionally, the varying molecular contamination on the optical blocking filter (OBF; see O'Dell et al. 2013; Plucinsky et al. 2018) of the ACIS detector leads to incorrect photon counts from standard data reduction methods, which needs to be accounted for. We added the HRC-S/LETG configuration since 2015 September for flux calibration purposes, as the HRC detector is not affected by this contamination.

We reprocessed and analyzed all previously published data taken between 1999 and 2015, and include them in this work for a self-consistent analysis of the entire data set. Following our approaches in Helder et al. (2013) and Frank et al. (2016), we exclude the earliest two observations, ObsIDs 1387 and 122, in our spectral analysis, as the focal plane temperature for those observations was higher than normal, and we have no corresponding charge transfer inefficiency correction available.[8] Additionally, they have an order of magnitude lower counts in the 0.5–8.0 keV band. Only imaging data are used at these epochs.

In this work, we analyze the zeroth-order images and spectra from ACIS-S/HETG observations to measure the evolving X-ray radii and fluxes, respectively. We use the zeroth-order HRC-S/LETG images and the first-order dispersed spectra (in the 0.5–2 keV band) to cross-check the residual pileup effects in the zeroth-order ACIS data.

For the data reduction, we adopt a similar procedure to that presented in our previous works (e.g., Burrows et al. 2000; Racusin et al. 2009; Park et al. 2011; Helder et al. 2013; Frank et al. 2016). We processed our entire data set between 2000 and 2023 with the `chandra_repro` script within CIAO version 4.15. We use the calibration database CALDB version 4.10.2 (with the latest ACIS-OBF molecular contamination models) for our spectral analysis. For each ACIS observation, we extracted the zeroth-order spectrum using the CIAO script `specextract` from a circular region with a radius of $\sim$4″ centered on the source. We extracted the background spectrum from an annular region with an inner radius of $\sim$6″ and an outer radius of $\sim$12″.

Since 2016, all of our Chandra observations of SNR 1987A at each epoch were split into multiple segments for effective telescope operations. Thus, for our spectral analysis, we combined the spectra of all individual ObsIDs for a given epoch. While the photon pileup is significantly reduced in the zeroth-order spectra thanks to the insertion of HETG, there remain some marginal pileup effects (typically with $\sim$5% of the total counts in the observed spectrum between 0.5 and 8.0 keV being affected by pileup[9]). To further combat these residual pileup effects, we used the ACIS pileup simulator (Broos et al. 2010) to synthesize the pileup-corrected ACIS

[8] https://cxc.cfa.harvard.edu/ciao/why/cti.html

[9] We choose not to use the terms "pileup fraction" or "pileup percentage" for defining this metric because the ACIS community has several conflicting definitions for those terms; see Section 1.2 in "The Chandra ABC Guide to Pileup" (http://cxc.harvard.edu/ciao/download/doc/pileup_abc.pdf).

Table 1
SNR 1987A: Chandra Observations, Fluxes, and Radii

Epoch	Age	ObsID[a]	Instrument	Exposure[b]	Counts[c]	0.5–2.0 keV Flux[d]	3.0–8.0 keV Flux[d]	Radius[e]
1999 Oct	4608	1387	ACIS-S/HETG	68.9	342	…	…	0.575 ± 0.024
2000 Jan	4711	122	ACIS	8.6	530	…	…	0.629 ± 0.022
2000 Dec	5036	1967	ACIS	98.8	8721	$2.76^{+0.05}_{-0.04}$	$0.74^{+0.06}_{-0.07}$	0.666 ± 0.007
2001 Apr	5175	1044	ACIS	17.8	1680	$3.04^{+0.08}_{-0.11}$	$1.04^{+0.22}_{-0.25}$	0.698 ± 0.015
2001 Dec	5406	2831	ACIS	49.4	5989	$4.20^{+0.06}_{-0.11}$	$0.96^{+0.12}_{-0.13}$	0.701 ± 0.008
2002 May	5560	2832	ACIS	44.3	6204	$5.20^{+0.07}_{-0.12}$	$1.16^{+0.16}_{-0.19}$	0.711 ± 0.008
2002 Dec	5789	3829	ACIS	49.0	8514	$7.37^{+0.11}_{-0.10}$	$1.30^{+0.11}_{-0.14}$	0.730 ± 0.007
2003 Jul	5978	3830	ACIS	45.3	9354	$9.42^{+0.12}_{-0.13}$	$1.57^{+0.14}_{-0.20}$	0.746 ± 0.007
2004 Jan	6157	4614	ACIS	46.5	11,527	$11.57^{+0.12}_{-0.12}$	$1.88^{+0.16}_{-0.31}$	0.754 ± 0.006
2004 Jul	6359	4615	ACIS	48.8	17,525	$14.78^{+0.14}_{-0.17}$	$1.99^{+0.17}_{-0.17}$	0.753 ± 0.005
2005 Jan	6530	5579	ACIS	31.9	15,864	$17.68^{+0.16}_{-0.21}$	$2.07^{+0.19}_{-0.18}$	0.746 ± 0.005
2005 Jul	6713	5580	ACIS	23.2	13,843	$21.93^{+0.21}_{-0.29}$	$2.67^{+0.32}_{-0.39}$	0.758 ± 0.006
2006 Jan	6913	6668	ACIS	42.3	30,161	$26.87^{+0.16}_{-0.24}$	$3.25^{+0.22}_{-0.25}$	0.755 ± 0.004
2006 Jul	7094	6669	ACIS	42.3	29,718	$31.91^{+0.10}_{-0.23}$	$3.54^{+0.22}_{-0.19}$	0.766 ± 0.004
2007 Jan	7270	7636	ACIS	33.5	31,990	$38.25^{+0.28}_{-0.32}$	$4.02^{+0.30}_{-0.27}$	0.770 ± 0.004
2007 Jul	7445	7637	ACIS	23.4	25,637	$43.02^{+0.49}_{-0.40}$	$3.66^{+0.23}_{-0.35}$	0.780 ± 0.004
2008 Jan	7624	9142	ACIS	6.4	7958	$47.22^{+0.76}_{-0.84}$	$4.09^{+0.69}_{-0.98}$	0.777 ± 0.007
2008 Jul	7799	9144	ACIS-S/HETG	42.0	5049	$52.39^{+1.22}_{-1.89}$	$5.02^{+0.29}_{-0.68}$	…
2008 Jul	7802	9143	ACIS	8.6	11,840	…	…	0.777 ± 0.006
2009 Jan	7987	10130	ACIS	6.0	8913	…	…	0.787 ± 0.007
2009 Jan	8000	10855	ACIS-S/HETG	18.8	2415	$57.20^{+2.13}_{-1.94}$	$5.40^{+0.64}_{-0.54}$	…
2009 Jul	8169	10222	ACIS-S/HETG	24.4	3450	$63.47^{+2.06}_{-1.67}$	$6.49^{+0.55}_{-1.52}$	0.776 ± 0.011
2010 Mar	8433	11090[f]	ACIS-S/HETG	24.6	3503	$65.16^{+2.02}_{-1.95}$	$6.64^{+0.57}_{-0.53}$	0.780 ± 0.011
2010 Sep	8617	13131[f]	ACIS-S/HETG	26.5	3954	$67.76^{+1.94}_{-2.49}$	$6.91^{+0.68}_{-1.15}$	0.785 ± 0.011
2011 Mar	8796	12539[f]	ACIS-S/HETG	52.2	8216	$70.97^{+1.24}_{-1.34}$	$8.16^{+0.38}_{-0.34}$	0.779 ± 0.007
2011 Sep	8975	12540[f]	ACIS-S/HETG	37.5	6133	$74.36^{+1.22}_{-1.83}$	$8.16^{+0.37}_{-0.38}$	0.779 ± 0.009
2012 Mar	9165	13735[f]	ACIS-S/HETG	42.9	7289	$81.48^{+1.66}_{-1.83}$	$8.97^{+0.69}_{-0.70}$	0.793 ± 0.008
2013 Mar	9523	14697	ACIS-S/HETG	67.2	11,674	$78.73^{+1.53}_{-1.50}$	$10.24^{+0.49}_{-0.40}$	0.809 ± 0.007
2013 Sep	9713	14698	ACIS-S/HETG	68.5	11,998	$82.56^{+1.45}_{-1.24}$	$11.50^{+0.29}_{-0.36}$	0.807 ± 0.006
2014 Mar	9885	15809	ACIS-S/HETG	70.5	12,051	$80.42^{+1.36}_{-1.30}$	$12.07^{+0.30}_{-0.38}$	0.813 ± 0.006
2014 Sep	10,071	15810	ACIS-S/HETG	47.9	8048	$83.38^{+1.68}_{-1.53}$	$11.83^{+0.60}_{-0.82}$	0.826 ± 0.008
2015 Mar	10,246	16757	HRC-S/LETG	67.6	6898	$82.58^{+3.33}_{-3.36}$	…	0.755 ± 0.009
2015 Sep	10,433	16756	ACIS-S/HETG	66.3	10,500	$82.52^{+1.64}_{-1.49}$	$12.72^{+0.59}_{-0.13}$	0.828 ± 0.007
2016 Mar	10,626	17898	HRC-S/LETG	68.6	8324	$83.03^{+3.18}_{-3.79}$	…	0.767 ± 0.014
2016 Sep	10,805	19882	ACIS-S/HETG	66.9	10,150	$85.20^{+1.67}_{-1.97}$	$14.52^{+0.57}_{-0.83}$	0.835 ± 0.009
2017 Mar	10,979	19290	HRC-S/LETG	67.6	8119	$82.01^{+3.98}_{-3.12}$	…	0.775 ± 0.011
2017 Sep	11,168	20793	ACIS-S/HETG	66.9	9189	$78.30^{+2.23}_{-2.57}$	$14.18^{+0.46}_{-0.76}$	0.833 ± 0.009
2018 Mar	11,351	21042	ACIS-S/HETG	313	39,783	$74.79^{+0.90}_{-0.92}$	$15.27^{+0.25}_{-0.23}$	0.847 ± 0.010
2018 Sep	11,527	20277	ACIS-S/HETG	67.2	8858	$75.58^{+2.23}_{-2.32}$	$14.95^{+0.65}_{-0.44}$	0.850 ± 0.011
2019 Mar	11,716	22155	HRC-S/LETG	77.6	9233	$74.68^{+3.93}_{-3.45}$	…	0.779 ± 0.014
2019 Sep	11,849	21304	ACIS-S/HETG	81.7	9682	$72.43^{+2.40}_{-2.25}$	$16.55^{+0.73}_{-0.51}$	0.861 ± 0.011
2020 Mar	12,087	23198	HRC-S/LETG	84.6	10,173	$71.70^{+3.32}_{-2.97}$	…	0.784 ± 0.011
2020 Sep	12,255	22425	ACIS-S/HETG	89.9	10,209	$70.68^{+1.85}_{-1.78}$	$17.92^{+0.58}_{-0.43}$	0.862 ± 0.009
2021 Mar	12,440	24653	HRC-S/LETG	58.6	6811	$69.26^{+3.94}_{-4.28}$	…	0.786 ± 0.013
2021 Oct	12,666	24654	ACIS-S/HETG	87.7	9299	$69.51^{+1.85}_{-1.78}$	$16.86^{+0.54}_{-0.52}$	0.868 ± 0.014
2022 Sep	12,995	25514	ACIS-S/HETG	83.4	8595	$69.44^{+2.07}_{-1.91}$	$17.74^{+0.52}_{-0.58}$	0.871 ± 0.010
2023 Apr	13,197	27495	HRC-S/LETG	40.9	4701	$66.16^{+5.75}_{-4.48}$	…	0.814 ± 0.022

Notes. 90% confidence intervals and 1σ errors are the quoted uncertainties for flux and radii measurements, respectively. The horizontal line after 2015 September separates the published and new observations used in this work.

[a] Only the longest ObsID in every epoch shown.

[b] Total exposure of all ObsIDs in an epoch used for flux measurement.

[c] Counts in the ACIS zeroth-order spectra and LETG first-order $(+1/-1)$ spectra in 0.5–8.0 keV energy band.

[d] X-ray fluxes in units of 10^{-13} erg s^{-1} cm^{-2}.

[e] X-ray radius (in arcseconds) measured only from the longest ObsID in the epoch.

[f] ACIS observations with a Science Instrument Module (SIM) offset of ∼8 mm along $-Z$-axis.

spectra for each epoch, following the approach as described in Helder et al. (2013). From the HRC-S/LETG data, we extracted first-order dispersed spectra (positive and negative arms) with the CIAO script, `tgextract`. Both the zeroth-order spectra (from ACIS observations) and the first-order LETG spectra (from HRC-S/LETG observations) were rebinned to have at least 30 counts per energy channel. For our spectral analysis we use version 12.13.0c of the XSPEC software package (Arnaud 1996).

We performed our imaging analysis generally following methods that were used in our previous works (e.g., Burrows et al. 2000; Racusin et al. 2009; Park et al. 2011; Helder et al. 2013; Frank et al. 2016). Considering the Chandra astrometric uncertainties for the ACIS data of SNR 1987A ($\sim$0.″1—e.g., Park et al. 2002) and its angular size ($\sim$1.″6), directly combining Chandra images of SNR 1987A from multiple ObsIDs at each observation epoch is difficult. Thus, we used only the longest ObsID in each observation for our image analysis. The standard ACIS spatial resolution is $\sim$0.″5, but SNR 1987A has an angular size of $\sim$1.″6. Thus, it is barely resolved by the ACIS detector. For our imaging analysis, we apply the subpixel resolution and point-spread function (PSF)-deconvolution methods to improve the effective ACIS resolution, which has become a standard image processing method for the Chandra analysis of SNR 1987A (e.g., Park et al. 2011; Helder et al. 2013; Frank et al. 2016). The subpixel resolution based on split-pixel events (which is now part of the standard Chandra data processing with CIAO) may improve the effective ACIS resolution by $\sim$10% (Mori et al. 2001). We generated three subband images of subpixel resolution, with energy ranges of 0.3–8.0 keV (broad), 0.5–2.0 keV (soft), and 3.0–8.0 keV (hard) for each ACIS observation.

For the PSF deconvolution, we binned the raw ACIS images to the 1/4 pixel size in both X and Y dimensions to create a 158×158 pixel image. We performed Chandra Ray Tracer (ChaRT) simulations to obtain the best available PSF, assuming monochromatic energies of 0.92 keV, 2.3 keV, and 3.8 keV for soft, broad, and hard ACIS subband images, respectively.

HRC images have no energy resolution and smaller pixel scales than ACIS images (about one-quarter of the ACIS pixel size). We binned the HRC images to 0.954 pixel size in both the X and Y dimensions of the detector to create a similarly sized 158×158 pixel image. We also used ChaRT simulations to construct the best available HRC PSFs assuming a monochromatic energy of 1.5 keV, approximately corresponding to the mean of the photon energy band covered by the HRC.

For each ObsID, the simulated PSF was generated by combining the results of 10 iterations with the web-based ChaRT interface,[10] each done with a different random seed to reduce the overall noise in the PSF. All rebinned images were then deconvolved with the simulated PSFs using the Lucy–Richardson iterative algorithm (Richardson 1972; Lucy 1974) and smoothed by convolving with a Gaussian (FWHM $\sim$0.″1). The effective spatial resolution of the ACIS images after the PSF deconvolution is $\sim$0.″27, which is in agreement with the results presented in previous works (e.g., Park et al. 2011; Helder et al. 2013; Frank et al. 2016).

[10] https://cxc.cfa.harvard.edu/ciao/PSFs/chart2/runchart.html

3. Analysis and Results

3.1. Broadband Spectral Model Fits

We perform broadband spectral model fits for the zeroth-order ACIS-S/HETG ("ACIS spectrum" hereafter) and the first-order HRC-S/LETG ("LETG spectrum," hereafter) spectra listed in Table 1. Based on previous analyses of the ACIS spectra, it has been shown that the spectral model fits with two characteristic shock components are required to adequately describe the X-ray emitting plasma in SNR 1987A (e.g., Park et al. 2005, 2006, 2011; Helder et al. 2013; Frank et al. 2016). X-ray emitting plasma in SNR 1987A has been shown to have significant nonequilibrium effects from the high-resolution Chandra gratings spectral analyses (Zhekov et al. 2006, 2009; Dewey et al. 2008; Bray et al. 2020; Ravi et al. 2021). Thus, we fitted the ACIS and LETG spectra with a two-component plane-parallel shock model (`vpshock` in XSPEC) that takes into account the NEI effects in an optically thin hot plasma (Borkowski et al. 2001).

We note that the early observation in 2001 April (ObsID: 1044) has a significantly lower number of counts (by several times or more compared to those at other epochs; Table 1). Due to these poor count statistics, a single-component spectral model was sufficient to fit the broadband spectrum with an averaged gas temperature (e.g., Park et al. 2011; Helder et al. 2013; Frank et al. 2016). In our spectral model fits, we implement the NEI version 3.0 in XSPEC, based on atomic database values in AtomDB v3.0.9.[11] We show the observed ACIS spectra with our best-fit two-component shock model at several representative epochs in Figure 1.

For the LETG spectra, we fit the first-order dispersed spectrum (both of the positively and negatively dispersed spectra), simultaneously. To model the higher-resolution emission lines in the grating spectra we convolved the two-component shock models with a Gaussian smoothing model (`gsmooth`) as demonstrated previously in the literature (e.g., Zhekov et al. 2006, 2009).

In our spectral model fits, we allowed the electron temperatures (kT, where the Boltzmann constant $k = 1.38 \times 10^{-23}$ J K^{-1} and T is the temperature in kelvin), ionization ages ($\tau = n_e t$, where n_e is the electron density of the shocked gas and t is the time since the gas was shocked), and normalizations of both components to vary. Hereafter, the lower kT among the two characteristic model components is termed the soft component, and the higher kT is the hard component.

In spectral model fits of the ACIS data taken in 2020 September, we found that the best-fit electron temperature for the soft component ($kT_{\rm soft} = 0.45^{+0.21}_{-0.16}$ keV) was abruptly lower than those estimated in the last several years (typically $kT_{\rm soft}$ $\sim$0.7–0.9 keV) but with larger uncertainties. We repeated our spectral model fits for this particular data set with $kT_{\rm soft}$ fixed at 0.78 keV, the best-fit electron temperature that we measured for our first-order LETG spectrum taken in 2020 March, the closest epoch to 2020 September among our Chandra monitoring observations of SNR 1987A. We found that these two spectral model fits (χ^2_ν: 196/182 v/s 200/183) are statistically indistinguishable (F-test probability $\sim$0.05) and thus consider it as a statistical fluctuation. In this work, we adopt the results from the latter fits (with $kT_{\rm soft} = 0.78$ keV), because we concluded that the abrupt change of $kT_{\rm soft}$ $\sim$0.45 keV only in

[11] http://atomdb.org/

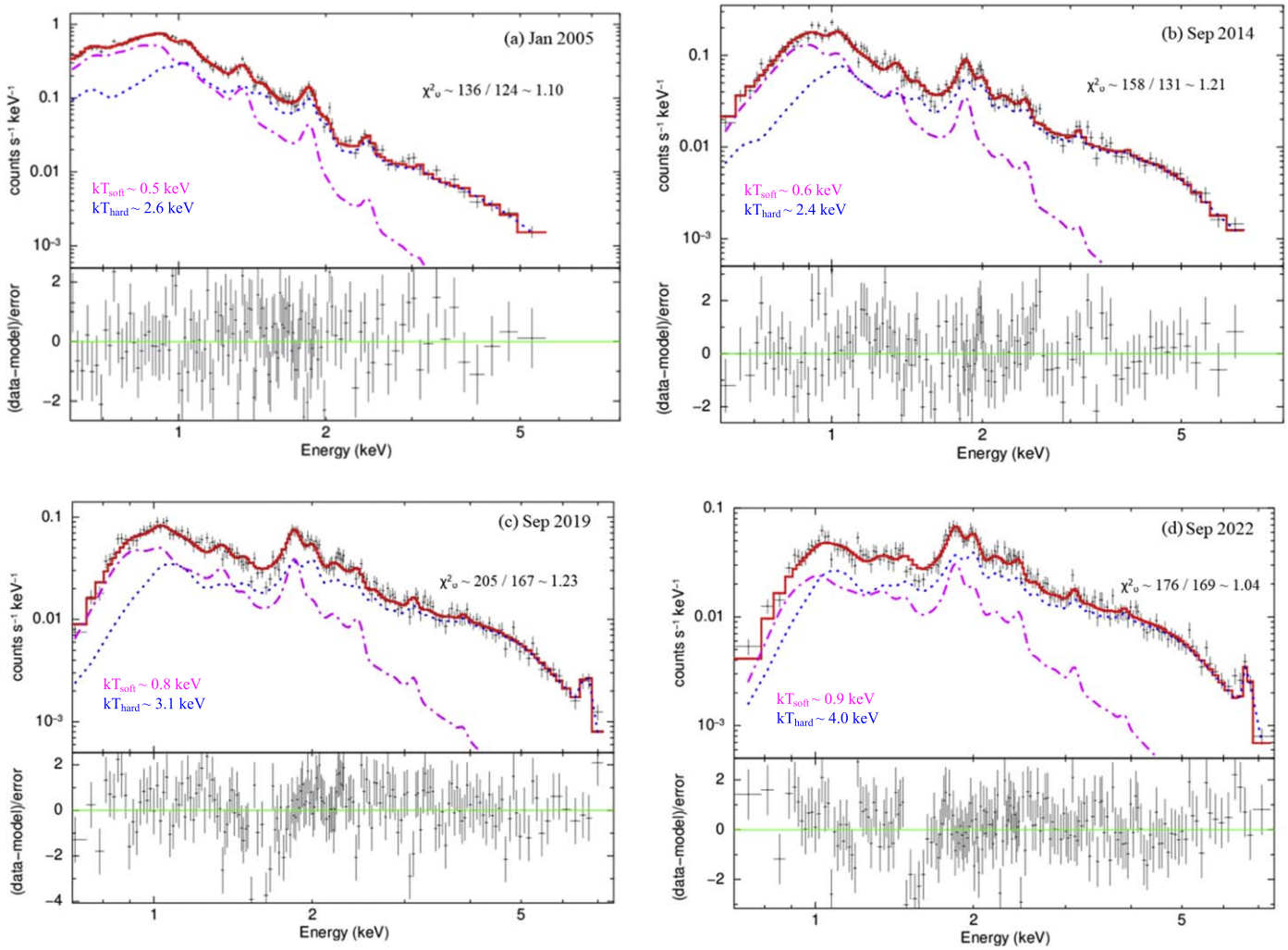

Figure 1. Best-fit two-component models (in red) and observed ACIS-S/HETG zeroth-order combined spectra (in black) in (a) 2005 January, (b) 2014 September, (c) 2019 September, and (d) 2022 September. The soft and hard model components are shown as dotted–dashed (in magenta) and dotted (in blue) lines, respectively. Postshock electron temperatures associated with the soft and hard components are marked. The reduced χ^2_ν value associated with the best-fit model is shown in each panel.

the single epoch of 2020 September may be physically unrealistic. Nonetheless, the best-fit model with $kT_{\rm soft} = 0.45$ keV involves large uncertainties, and thus, our scientific outcomes are not affected by accepting either result.

The total absorption column in the direction of SNR 1987A was fixed at $N_{\rm H} = 2.17 \times 10^{21}$ cm^{-2} (Ravi et al. 2021). All abundances are relative to the solar abundance table by Asplund et al. (2009)—`aspl` in XSPEC. Initially, we fixed the following elemental abundances for SNR 1987A: He = 1.98 (Mattila et al. 2010), C = 0.12 (Fransson et al. 1996), N = 0.92, O = 0.14 (Zhekov et al. 2009), Ne = 0.34, Mg = 0.25, Si = 0.36, S = 0.40, and Fe = 0.19 (Ravi et al. 2021). Further, we also fix Ar = 0.776, Ca = 0.354, and Ni = 0.662 at their respective LMC values (Russell & Dopita 1992). We tie all the elemental abundances between the soft and hard components. With these spectral model fits, we are able to describe the observed spectra that we obtained until ∼2016. These results are in agreement with the previously published results in Frank et al. (2016).

Starting in 2018 March, we detect emission from a clear line-like feature at ∼6.7 keV, likely due to the presence of the Fe K line complex. The detection of Fe K emission line features has been reported in the XMM-Newton (XMM) data since ∼2009 (e.g., Sturm et al. 2010; Maggi et al. 2012; Sun et al. 2021), and here we confirm it with our Chandra data. We find that fixing the Fe abundance at the ER value (0.19) during these epochs significantly underestimates the observed fluxes at ∼6.7 keV. In Figure 2(a), we show the ACIS spectrum taken in 2022 September overlaid with the spectral model fits with the Fe abundances fixed at the ER value. In Figure 2(b), we present the ACIS spectrum from the same epoch, with the Fe abundance associated with the hard model component allowed to vary. Fitting the Fe abundance in the hard-component model improves the broadband spectral fit ($\chi^2_\nu = 184/170$ to $\chi^2_\nu = 175/169$), for which an F-test indicates a marginal improvement (F-probability $\sim 3 \times 10^{-3}$). While the overall broadband fit improvement by allowing the hard-component Fe abundance to vary is marginal, this may be misleading, as our feature of interest is a narrowband region around the Fe K emission line. We discuss the narrow band in more detail in Section 3.3. It is rather clear that the improvement in the model fit is significant in the Fe K line band (Figure 2(b)).

The measured Fe abundance associated with the hard component is a factor ∼2–3 higher than the previously

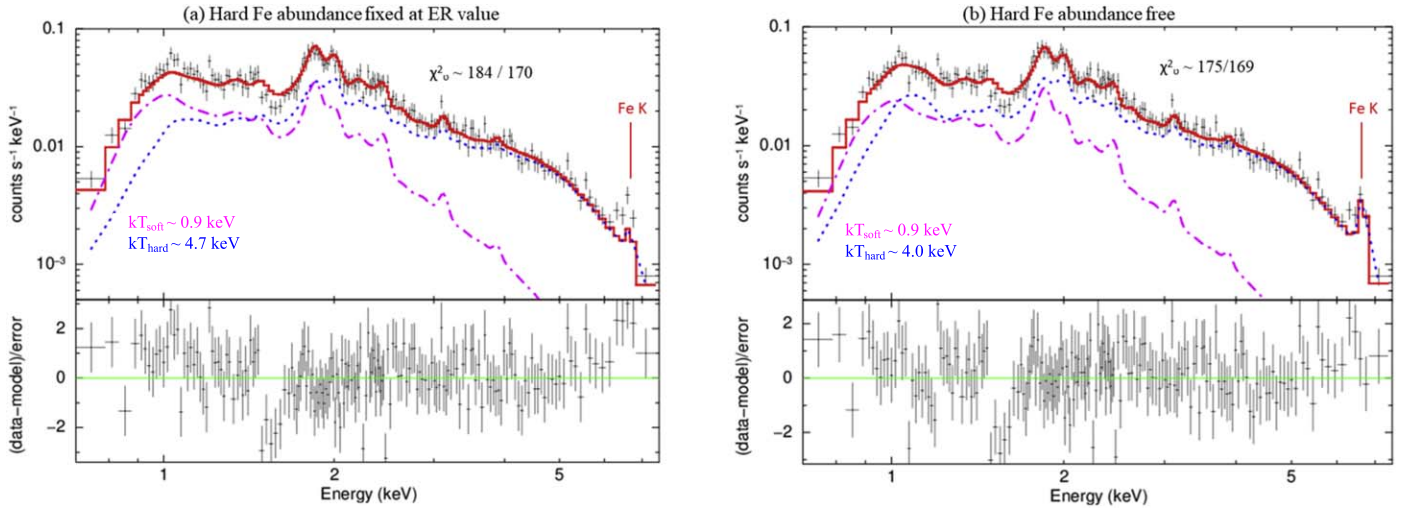

Figure 2. Best-fit two-component model (in red) and observed zeroth-order spectrum (in black) from the latest ACIS-S/HETG observation in 2022 September (ObsID: 25514). Plot schemes for soft and hard components are the same as in Figure 1. In panel (a), all abundances for both soft and hard components are fixed at ER values. The Fe K line complex at ∼6.7 keV (marked in red) is underestimated in the left panel. In panel (b), the Fe abundance associated with the hard component is allowed to vary while all other abundances are fixed at ER values.

measured Fe abundances of the ER with Chandra (Zhekov et al. 2009; Ravi et al. 2021). However, this abundance enhancement has large measurement uncertainties and could be consistent with the average Fe abundances of LMC stars (e.g., Urbaneja et al. 2017; Romaniello et al. 2022), making it statistically marginal.

The associated evolution of the hard-component electron temperature during this period is shown in Figure 3. We observe a marginal linear increase (within uncertainties) in the hard-component postshock electron temperature. The more energetic electrons can excite the Fe XXV line complex significantly, resulting in an increase in its line intensity. Our observations strengthen the case for the presence of a He-like Fe XXV line complex. We note that if the X-ray emitting plasma is in NEI, then the emission from He-like triplets is enhanced. This is consistent with our assumptions that the NEI effects are strong in the X-ray-emitting plasma in SNR 1987A. As electron temperatures and abundances are varied simultaneously, there can be cross-correlation between their results, and thus it is important to implement more complex and independent models to better constrain the potentially increasing Fe abundance in SNR 1987A.

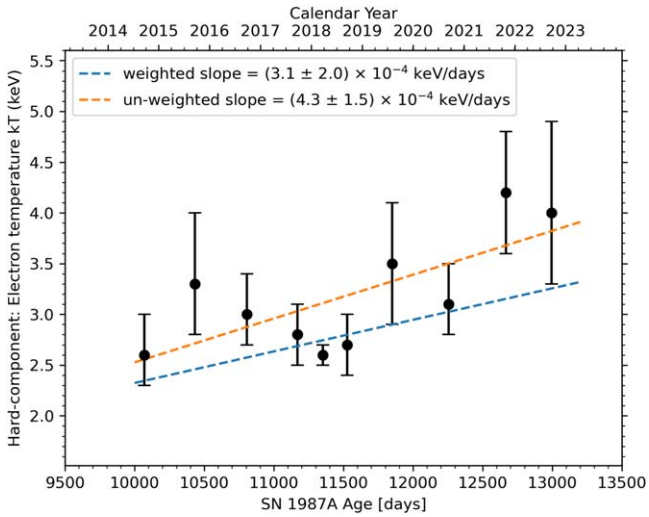

Figure 3. Measured electron temperatures associated with the hard component between 2016 September and 2022 September. The best-fit line considering weighted data (slope = $(3.1 \pm 2.0) \times 10^{-4}$ keV day^{-1}) is shown with a dashed blue line, while the linear fit based on unweighted data (slope = $(4.3 \pm 1.5) \times 10^{-4}$ keV day^{-1}) is shown with a dashed orange line. A marginal linear increase with the weighted data suggests that the increasingly significant line around ∼6.7 keV is likely due to the He-like triplet Fe XXV.

3.2. X-Ray Light Curves

In Table 1, we list our X-ray flux measurements based on our two-component spectral model fits to the ACIS and LETG spectra. An important systematic point of consideration in the ACIS flux measurements has been the temporal changes of the soft X-ray transmission of the ACIS OBF due to the deposition of contaminants on its surface (O'Dell et al. 2013; Plucinsky et al. 2018). This contamination is strongest below 1 keV. To account for this artifact, we created the detector response maps for all of our new observations (taken since 2016) based on the calibration database with the latest ACIS-OBF contamination models (see Section 2). We also recreated the detector responses for all previously published data (taken before 2016) with the same calibration database for self-consistent flux measurements throughout the entire epochs.

To cross-check our soft X-ray flux measurements with the ACIS data, we measure the 0.5–2.0 keV band flux with the first-order HRC-S/LETG spectra, which are free of both pileup and contamination. The measured fluxes from the LETG spectra between 2015 and 2023 are consistent with those that we measured based on our pileup-corrected ACIS spectra at corresponding epochs (within uncertainties), offering an independent verification and confidence in the true nature of the soft X-ray light curve.

The resulting 0.5–2.0 keV (soft) and 3.0–8.0 keV (hard) X-ray light curves are presented in Figure 4. All measured X-ray fluxes between 1999 and 2016 are consistent with the previously published results in Frank et al. (2016), within statistical uncertainties. We find that the evolution of the soft X-ray light curve has changed significantly since 2016. The measured soft X-ray fluxes between 2016 (∼10,800 days) and 2020 (∼12,200 days) decline roughly linearly (by ∼4.5% per year;

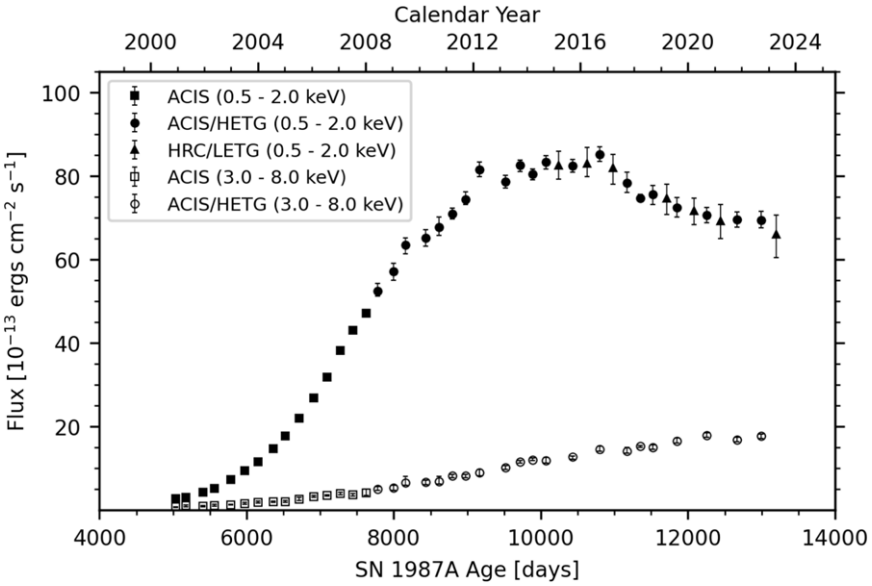

Figure 4. X-ray light curves of SNR 1987A between 1999 (5036 days) and 2023 (13,197 days). The softband (0.5–2.0 keV) fluxes are in filled markers, and the hardband (3.0–8.0 keV) fluxes are in open markers. For several points, the error bars are too small to be visible.

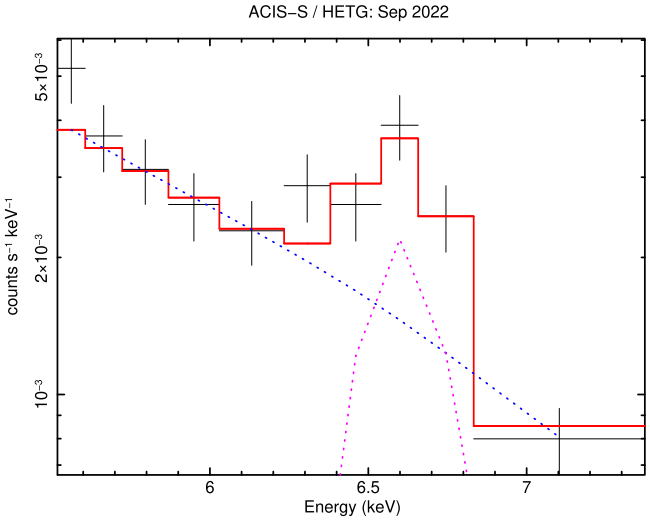

Figure 5. Absorbed power law + Gaussian fits to the Fe K line observed in 2022 September. The underlying continuum (characterized by a power law) component is in blue, and the Gaussian component in magenta. The overall best-fit model is in red.

Figure 4). Such a declining trend is generally consistent with the shock recently entering a low-density gas between 2011 and 2018, based on deep, high-resolution Chandra HETG spectra (Ravi et al. 2021). This recently declining soft X-ray flux has also been reported by the XMM observations during similar epochs (Sun et al. 2021). Since 2020, the soft X-ray flux appears to level off at around $\sim 7 \times 10^{-12}$ erg s^{-1} cm^{-2} (Figure 4). Upcoming Chandra monitoring observations will be crucial to test this latest trend in the evolution of the soft X-ray light curve.

In contrast, the hard X-ray light curve shows a steady increase until ~2020 (~12,200 days). Since 2020, the observed hard X-ray fluxes might show hints of leveling off. However, it is difficult to draw a firm conclusion on this latest change in the hard X-ray light curve. Follow-up Chandra monitoring observations are required to test the true shape of the hard X-ray light curve of SNR 1987A.

Table 2
Fe K Line Profiles

Epoch	Age (days)	Line Center (keV)	Line Equivalent Width (keV)	Line Flux (10^{-6} photons cm^{-2} s^{-1})
2018 Mar	11,351	6.65 ± 0.05	0.27 ± 0.08	3.9 ± 1.2
2018 Sep	11,527	6.70 ± 0.06	0.52 ± 0.18	7.0 ± 2.9
2019 Sep	11,849	6.72 ± 0.08	0.46 ± 0.16	7.3 ± 2.7
2020 Sep	12,255	6.63 ± 0.09	0.41 ± 0.16	6.7 ± 2.6
2021 Oct	12,666	6.69 ± 0.06	0.38 ± 0.15	6.3 ± 2.3
2022 Sep	12,995	6.61 ± 0.05	0.50 ± 0.13	8.9 ± 2.7

Note. All measured uncertainties are 90% confidence intervals.

3.3. Fe K Emission Line

The detection of Fe K emission lines has been previously reported by several studies with XMM and NuSTAR (e.g., Sturm et al. 2010; Maggi et al. 2012; Alp et al. 2021; Sun et al. 2021). These lines were not detectable in Chandra data prior to 2016 (Frank et al. 2016). In this work, we report the detection of an excess above the continuum around ~6.7 keV in the Chandra ACIS spectra, clearly identified first in March 2018 and then detected in every subsequent observation (Figures 1, 5).

To study the Fe K line profile and its temporal evolution, we fitted the 5.0–8.0 keV band ACIS spectra taken from 2018 March to 2022 September with an absorbed power law and a Gaussian model. Our best-fit model of the Fe K line profile in 2022 September is shown in Figure 5. Our best-fit line center, equivalent width, and line flux of the Fe K complex in each epoch between 2018 and 2022 are summarized in Table 2. The evolution of the Fe K line flux is presented in Figure 6. Even though the measured uncertainties are large (typically ~3σ detections), the Fe K line detection has been significant ever since 2018. We also include a few representative epochs of Fe K line fluxes measured with EPIC-pn (on XMM-Newton)

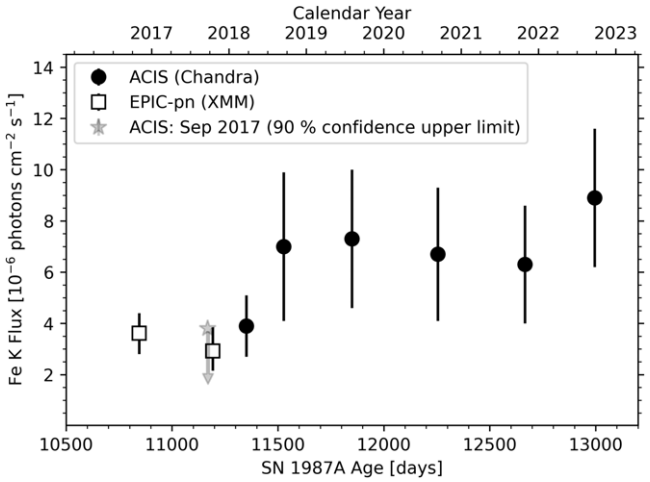

Figure 6. Measured Fe K line fluxes from ACIS zeroth-order spectra between 2018 and 2022 (Table 2). Two epochs of EPIC-pn (XMM) measurements from Sun et al. (2021) are also plotted. In 2017 September (day ∼11,168), only an upper limit was achieved from the ACIS data.

between 2015 and 2017 (Sun et al. 2021). Our measured Fe K line flux in 2017 September shows large statistical uncertainties, and thus we place an upper limit (90% confidence). We find a plausible agreement between the 2018 March Chandra and the 2017 October XMM result. Since 2018, our Chandra-measured Fe K fluxes have significantly increased. Concurrent XMM fluxes are not currently available in the literature but future works will be useful to compare with our Chandra results.

We also measure the line equivalent width based on our best-fit Gaussian model fits (Table 2). All of our measurements of the Fe K line fluxes, line equivalent widths, and Fe abundances consistently indicate the recent development of strengthening X-ray emission from the shocked hot Fe gas.

The measured mean line centroid energy of the Fe K profile in the ACIS spectra is 6.66 keV (Table 2). Based on XMM data, Sun et al. (2021) estimated the Fe K line centroid to be 6.67 keV at 12,000 days, which is in good agreement with our Chandra measurements in 2019–2021 (Table 2). A line centroid energy of ∼6.7 keV approximately corresponds to the ionization state Fe XXV, consistent with a thermal origin (Makishima 1986; Kallman et al. 2004). This identification of the Fe line is consistent with the evolution of electron temperatures associated with the hard component between 2016 and 2022 in our modeling (Figure 3). It is also consistent with previously reported XMM-based measurements in Alp et al. (2021). In general, the overall observed Fe K complex is most likely a result of the contributions of differently ionized Fe species. Thus, our results may indicate that the true evolution of the Fe K line is due to a progressive ionization from the earlier detection by Maggi et al. (2012).

3.4. X-Ray Images

The superb angular resolution of Chandra offers a unique opportunity to resolve and study the changing morphology of SNR 1987A in X-rays. The evolution of Chandra ACIS images between 2000 and 2022 is shown in Figure 7. The ER was initially brighter in the east but became brighter in the west after ∼2010 (∼8500 days after SN) (Park et al. 2011; Frank et al. 2016). The change in the E–W brightness of the X-ray remnant is consistent with the temporal sequence of optical spots (e.g., Sugerman et al. 2002; Fransson et al. 2015), which supports the asymmetric propagation of the blast wave between east and west. The recent ACIS image in 2022 (∼13,000 days) suggests that the western half has also dimmed since 2016, which is generally consistent with the declining soft X-ray light curve for the same period (Figure 4).

3.5. Radial Expansion Rate

The high cadence of ACIS observations, coupled with excellent spatial resolution, enables us to track the changes in the X-ray radial expansion of SNR 1987A. We measure the radius of the X-ray emitting ring and its thickness by adopting similar methods to those described in Racusin et al. (2009). In these methods, we fit each deconvolved ACIS image to an image model that consists of four representative lobes and an underlying uniform ring. The estimated radius represents the average distance from the center to the peak X-ray emission in SNR 1987A. The thickness of the independent lobes is a free parameter in our image model, which is averaged out to get the width of the X-ray-emitting ring.

The best-fit radii of the broadband images are shown in Figure 8(a) and Table 1. We also measured the radius for soft- and hardband images to study the energy dependence of the X-ray radius (Figure 8(b)). For each band, epochs with at least several hundred counts were included in the radial expansion analysis to ensure statistically reliable measurements. Applying a similar image modeling to that we used for the ACIS images (e.g., Racusin et al. 2009; Park et al. 2011; Helder et al. 2013; Frank et al. 2016), we measured the SNR's radii based on our zeroth-order HRC data for several epochs between 2015 and 2023 (Table 1).

Because three different detector modes (bare ACIS, ACIS/HETG zeroth order, and HRC/LETG zeroth order) are used to measure the angular size of SNR 1987A down to ∼arcsecond scales, we cross-calibrate to test any systematic effects in our measurements among these configurations. Measured radii with bare ACIS configuration are systematically higher (by ∼2%) than the corresponding ACIS-S/HETG configurations. This small systematic effect was not identified in our previous work (Frank et al. 2016). While Frank et al. (2016) used an older version of PSF created by MARX, we used the up-to-date PSF created by ChaRT (using SAOTrace[12] Carter et al. 2003), which is probably a more accurate description. SAOTrace is a high-fidelity ray tracer for the Chandra mirrors that simulates many details that are treated statistically in MARX to improve efficiency. The two Chandra epochs between 2008 and 2009 (when HETG was first inserted) were observed with both the bare ACIS and the ACIS-S/HETG configurations (ObsIDs: 9143, 9144 and ObsIDs: 10130, 10855—Table 1). We estimated the cross-calibration factor between ACIS and ACIS-S/HETG configurations based on radii measurements at these epochs.

Measured radii with HRC are systematically lower than their corresponding ACIS epochs (by ∼9%), indicating systematic effects between two different types of detectors (including differences in their spatial resolutions). Nonetheless, the SNR's expansion rate in HRC images is consistent with that in ACIS images (within statistical uncertainties) between 2016 and 2022, providing an independent confirmation of the radial expansion rate of SNR 1987A that we measure with the ACIS

[12] https://cxc.harvard.edu/cal/Hrma/SAOTrace.html

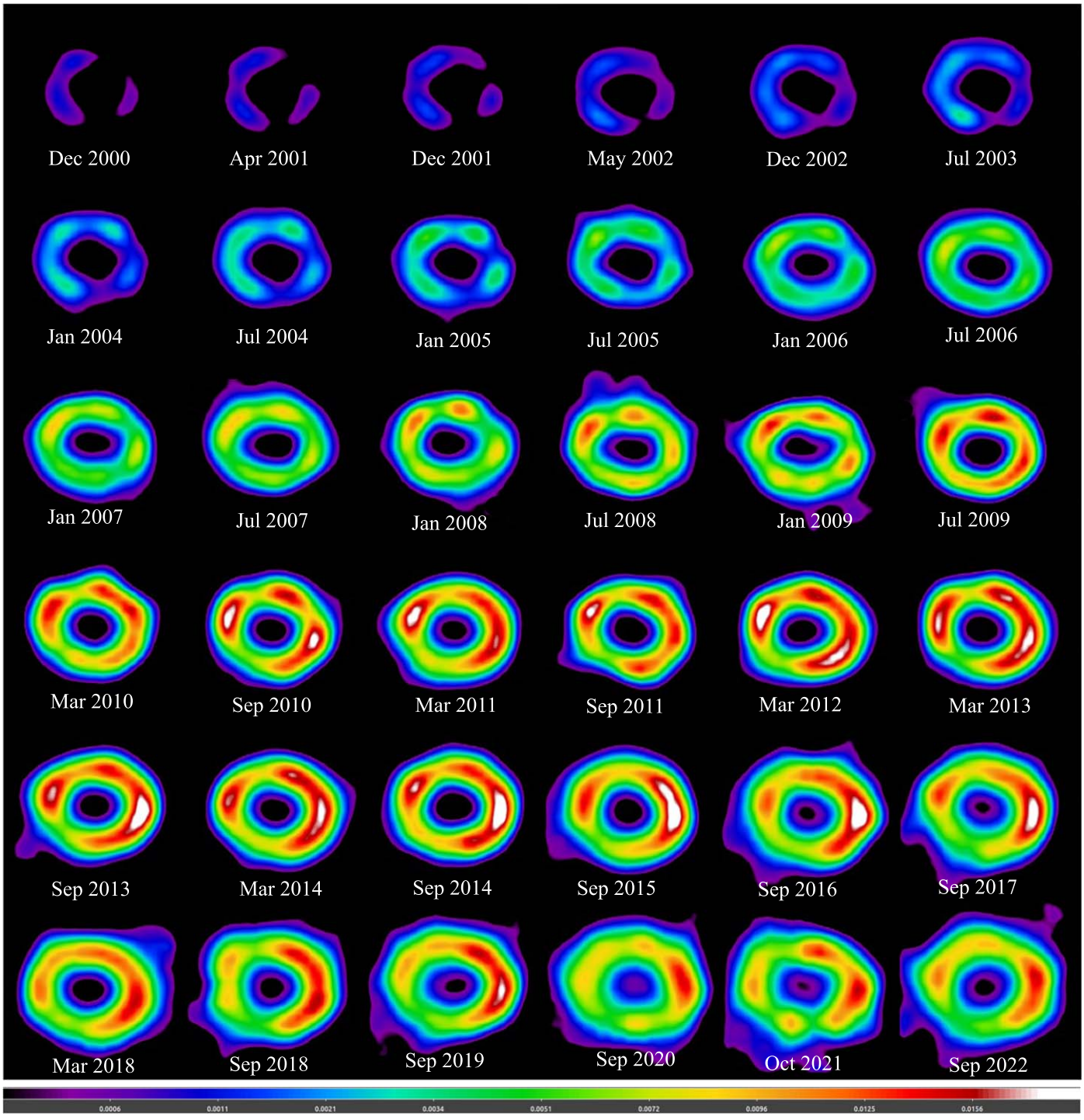

Figure 7. Deconvolved and smoothed broadband (0.3–8.0 keV) false-color Chandra ACIS images of SNR 1987A between 2000 December (day 5036) and 2022 September (day 12,995). All images are normalized by flux and use a square root scale on the same color scale (bottom). In all images, north is up, and east is to the left.

images (see below). The HRC images are scaled up by ∼9% and fit together with the ACIS images to estimate the late-time (since ∼2004) velocity, $v_{\rm late}$ in Figure 8(a).

We estimate the early velocity, $v_{\rm early}$ of the expanding broadband images before the strong shock interaction with the ER at around 2004 as $6700 \pm 750\,{\rm km\,s^{-1}}$, and it reduces to $1830 \pm 40\,{\rm km\,s^{-1}}$ after 2004. Our refined measurements of expansion rates are consistent (within uncertainties) with earlier results of Racusin et al. (2009), Helder et al. (2013), and Frank et al. (2016). Since 2016, the overall expansion rate of SNR 1987A continues to show a linear rate similar to that estimated for the period of 2004–2015. Thus, the bulk of broadband X-ray emission still appears to be dominated by emission from the shocked dense CSM in the ER until 2022.

In Figure 8(b) we compare the energy dependence of the expansion rate between soft, hard, and broadband ACIS images. The softband expansion (in green) is similar to the broadband expansion (in black) until ∼2016, indicating that the

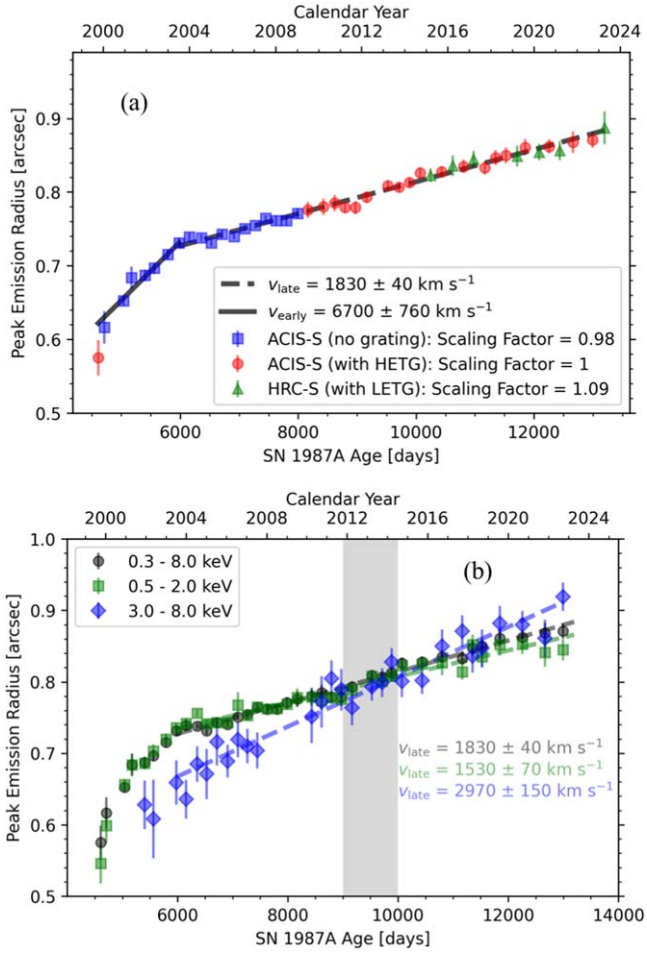

Figure 8. (a) Best-fit radii of the 0.3–8.0 keV broadband ACIS images and HRC images between 1999 and 2023. A broken linear fit describes the expansion rate before and after the shock hitting the main body of the ER in 2004. Measured bare ACIS radii are scaled down by ∼2%, and HRC radii are scaled up by ∼9%, which accounts for the cross-calibration in the radius measurements between bare ACIS and ACIS-S/HETG configurations and HRC-S/LETG and ACIS-S/HETG configurations, respectively (see Section 3.5). (b) Comparisons of the best-fit radii of SNR 1987A among the soft (0.5–2.0 keV), hard (3.0–8.0 keV), and broadband (0.3–8.0 keV). A vertical band (gray) shows the period between ∼2012 and 2015, where the soft, hard, and broad energy band images have similar best-fit radii.

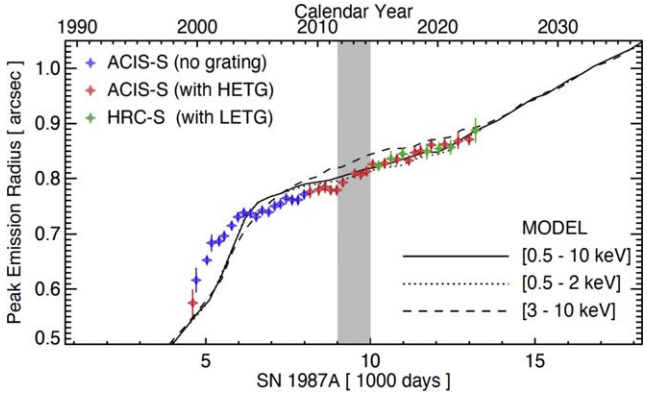

Figure 9. Comparison between best-fit radii of the 0.3–8.0 keV broadband ACIS images and HRC images between 1999 and 2023 with MHD model-predicted expansion rates in 0.5–10.0 keV (solid), 0.5–2.0 keV (dotted), and 3.0–10.0 keV (dashed) energy bands. A vertical band (gray) shows the period between ∼2012 and 2015, where the soft, hard, and broad energy band observed images have similar radii. General trends among the model expansion rates are consistent with observations.

softband emission was dominating the broadband image. Since ∼2016, the softband radius appears to become smaller than the corresponding broadband radius. In fact, our linear expansion model fits show that the expansion rate (1530 ± 70 km s^{-1}) in the softband images is slightly lower than that (1830 ± 40 km s^{-1}) in the broadband images (Figure 8(b)).

The hardband expansion rate has been steeper (than soft/broadband rates) throughout the entire period of our measurements. The radius of the hardband image was significantly smaller compared to respective broadband images at early epochs, but it caught up with the broad/softband size in ∼2012–2015 (∼9000–10,000 days, Figure 8(b)). This epoch is coincident with the period when the soft X-ray light curve leveled off (Figure 4). By 2018 (∼10,300 days), the hardband images have started to overtake the broadband emission size. In 2022 (∼13,000 days), the hardband image is clearly larger than either of the soft or broad X-ray images of SNR 1987A (Figure 8(b)). A fit between 2004 and 2022 of the hardband images gives an expansion rate of 2970 ± 150 km s^{-1}, which is significantly faster than the peak emission expansion rate observed from the broadband images for the same time period.

In Figure 9, we compare the radial expansion rates from observations (ACIS broadband images and HRC images) with the MHD model-predicted expansion rates. The radius in the model hard band (3–10 keV) is initially smaller than in the model soft band (0.5–2.0 keV), eventually becoming larger like their observed counterparts. The slope in the model hard band during the interaction with the dense ring is steeper than in the model soft band because the shock velocity in the H II region and less-dense interclump material (which mainly contributes to the hard X-ray emission) is higher than the shock velocity in the densest component of the ring (contributing to the soft X-ray emission). The soft model component closely tracks the broadband model component, suggesting that peak X-ray emission is still dominated by the dense ER. Thus, the predicted MHD model evolution of the X-ray radii at different energies is consistent with the observed subband trends (Figure 8). The discrepancies present between model-predicted radii and observations could be due to the assumed density structure of CSM in the model, and our observations will be useful in constraining these assumptions. However, qualitatively, the model replicates our observed trends, supporting the physical picture of SNR 1987A's evolution. The model further predicts a notably steeper expansion rate both presently and in the future. This is attributed to the faster expansion of the remnant in the less-dense CSM beyond the ring. Once again, this aligns with the physical picture emerging from our observations.

4. Discussion

4.1. X-Ray Emitting Plasma: Light Curves and Fe Abundance

The physical conditions of the X-ray emitting plasma have been approximately modeled with a characteristic bimodal temperature distribution of plane-parallel shocks in the literature (e.g., Frank et al. 2016). The cool ($kT = 0.3$–0.9 keV) or soft component represents X-ray emission primarily from the shocked dense clumpy materials in the ER, while the hot ($kT = 1.5$–3.0 keV) or hard component describes the combination of X-ray emission from within the interclump gas in the

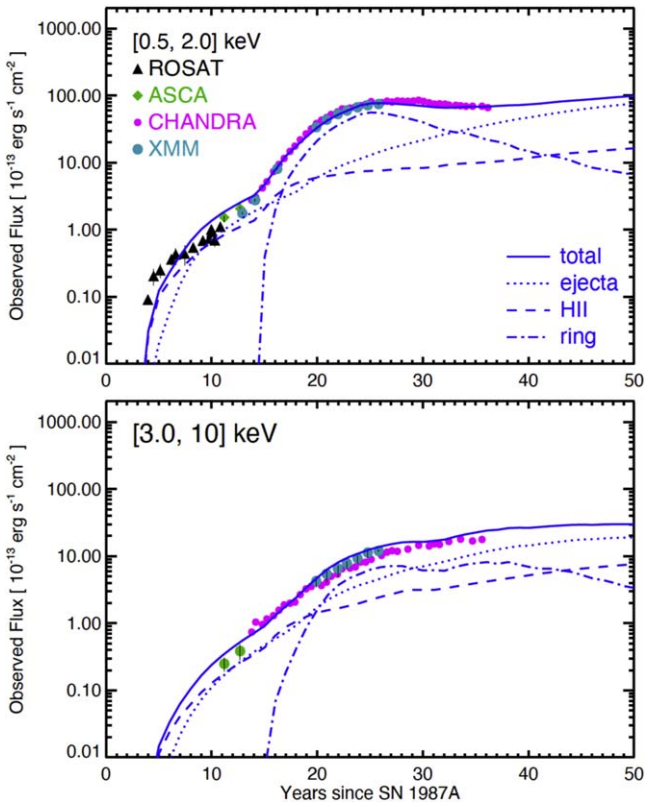

Figure 10. Top: Comparison between observed soft X-ray fluxes and corresponding MHD-simulated model components (Orlando et al. 2020). Chandra fluxes (magenta) are from this work, XMM fluxes (blue) from Haberl et al. (2006), Maggi et al. (2012), ROSAT fluxes (gray) from Haberl et al. (2006), and ASCA fluxes (brown) from Appendix B of Orlando et al. (2015). The MHD model predicts that the soft X-ray flux from the shocked ejecta (dotted) may become more significant than that from the shocked ER (dotted–dashed) in $\gtrsim$2022 ($\gtrsim$35 yr). Bottom: Similar comparison between observed hard X-ray fluxes and the corresponding MHD-simulated model components.

ER and from the shocked less-dense material from the H II region (Zhekov et al. 2010; Orlando et al. 2015).

Since 2011, the soft X-ray flux from SNR 1987A has leveled off at $\sim 8 \times 10^{-12}$ erg s^{-1} cm^{-2} (Frank et al. 2016). Such a flattening has been previously predicted to be an indicator of the blast wave starting to move out of the dense ER (Park et al. 2011; Dewey et al. 2012; Orlando et al. 2015). We find that the soft X-ray light curve started to decline roughly linearly since 2016, decreasing to $\sim 7 \times 10^{-12}$ erg s^{-1} cm^{-2} by $\sim$2020. This new feature in the soft X-ray light curve is consistent with the physical interpretation in which the forward shock's propagation beyond the ER has become significant, heating hitherto unknown low-density CSM. Since 2020, we find that the soft X-ray light curve appears to have stopped declining, and leveled off. This latest development in the soft X-ray light curve of SNR 1987A is in plausible agreement with the MHD model predictions (Orlando et al. 2020, and Figure 10), in which the emerging X-ray emission from the reverse-shocked ejecta is expected to cause a similar change in the soft X-ray light curve.

The MHD model predicted that the X-ray flux from the reverse-shocked outer layers of ejecta would grow to be the dominant component in the soft X-ray spectrum in $\sim$2022 or later. Based on these MHD models, the reverse shock is currently traveling through the extended H envelope and the underlying He envelope. According to the stellar evolution model used in these SN–SNR simulations, the mass of these H and He envelopes is about 10 $M_{\odot}$ (Ono et al. 2020). So, the shocked ejecta in the MHD models are mainly shocked material from these envelopes. As the reverse shock travels further into the ejecta, significant changes in the X-ray spectrum of SNR 1987A (i.e., developments of strong emission lines from the shocked heavy ions such as Si, Fe, O, etc.) are expected in the near future due to the expected dominating contribution from the reverse-shocked metal-rich ejecta.

Our observations of the increasing Fe K line flux may indicate the onset of X-ray emission from the reverse-shocked ejecta. However, the current results from Chandra data are insufficient to distinguish them from a CSM origin. Compared with MHD simulations (Orlando et al. 2020), we find that the contributions from both the ejecta component and the ring component (CSM) are comparable at this stage (see Figure 10). These simulations suggest that the shocked ejecta originate from the outer layers rich in H and He, while the Fe-rich ejecta in the innermost layers exhibit significant asymmetry due to the bipolar explosion (Ono et al. 2020; Orlando et al. 2020). This asymmetry results in the extension of Fe-rich plumes through the outer layers of ejecta, bringing them closer to the reverse shock. Current models predict that these Fe-rich plumes have not yet started the interaction with the reverse shock. However, recent observations with JWST NIRSpec of SNR 1987A have unequivocally detected this asymmetry[13] and suggested that the Fe-rich plumes have already begun interacting with the reverse shock (Larsson et al. 2023). Follow-up Chandra monitoring observations are therefore essential to validate these observed trends at X-ray wavelengths and provide observational constraints to improve the explosion models.

4.2. Asymmetry of Fe K Emission

Chandra X-ray images showed the brightening in the eastern side first, and then in the western side subsequently (around 2010; Figure 7). Similar time sequences have been recognized in the developments of optical hot spots and radio lobes (Sugerman et al. 2002; Ng et al. 2013; Zanardo et al. 2014; Fransson et al. 2015). These multiwavelength observations may indicate an asymmetric progress of the blast wave between the eastern and western sides of the SN, probably due to an asymmetric explosion and/or nonuniform CSM distribution. In either scenario, an asymmetric progress of the reverse shocks between the eastern and western sides of the SNR would be expected, which may accordingly result in time-differential developments of the X-ray emission from the reverse-shocked ejecta between the eastern and western halves of the SNR.

Motivated by the recent development of the Fe K emission line, the hints of enhanced Fe abundance, and the JWST observations (Larsson et al. 2023), we may entertain the scenario that the strengthening Fe K emission line is due to reverse-shocked ejecta. Considering the asymmetric developments of X-ray emission between the eastern and western regions of SNR 1987A, we may also expect an asymmetry in the Fe K line flux due to a similar asymmetric development of the reverse shock between the eastern and western halves.

To test this scenario, we measured the Fe K line fluxes from the eastern and western halves of SNR 1987A between 2018 and 2022 (Figure 11). While uncertainties are large due to low

[13] Previously, Larsson et al. (2016) discussed the ejecta asymmetry of SNR 1987A at optical and near-infrared wavelengths.

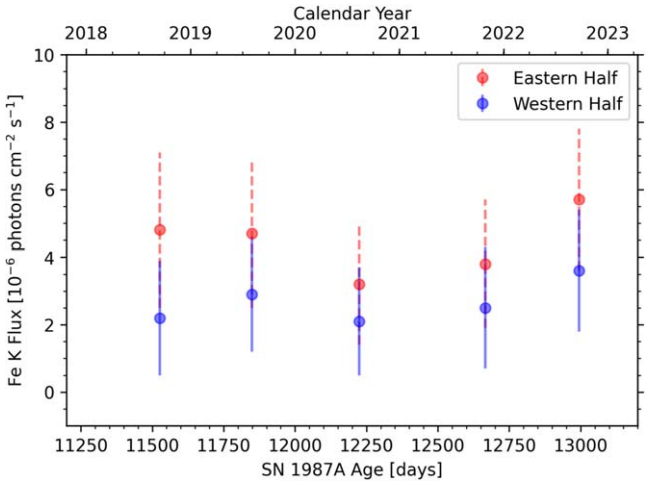

Figure 11. Fe K flux measured from the eastern and western halves of SNR 1987A between 2018 and 2022.

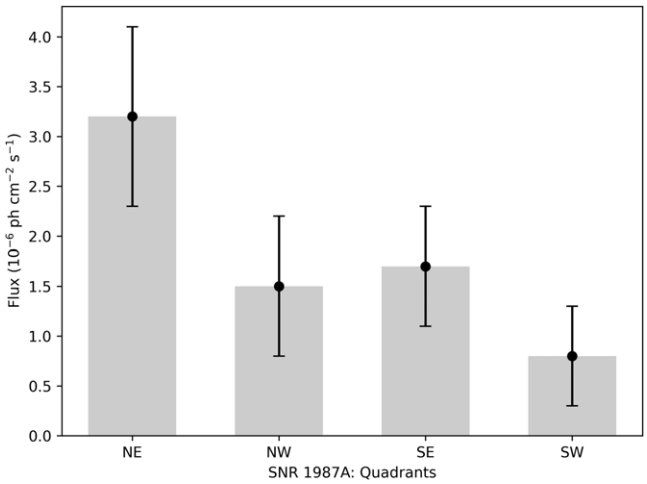

Figure 12. Fe K flux measured in the combined spectra (between 2020 and 2022) from northeast (NE), northwest (NW), southeast (SE), and southwest (SW) quadrant regions of SNR 1987A. Fluxes are measured as described in Section 3.1. Uncertainties are 90% confidence intervals.

count statistics in the Fe K line features extracted from eastern and western halves, it is interesting to find that the best-fit Fe K line flux is ∼twice as high in the eastern half at all epochs. This systematic spatial distribution of the Fe K line flux is supportive of our assumed physical picture of the Fe K line originating from the asymmetric reverse-shocked ejecta. However, the alternate scenario of enhanced Fe fluxes due to changing thermal conditions of an asymmetric CSM origin between eastern and western halves is equally feasible. As the contribution of the emerging emission from the shocked ejecta in the X-ray spectrum is expected to become more significant in the future, continuing Chandra observations will present a unique opportunity to test the hypothesis of such an asymmetric development of the reverse shock in SNR 1987A.

We combine all ACIS data taken from 2020 to 2022 (where we see the enhanced Fe K line fluxes, Figures 4 and 10) to increase photon count statistics in the Fe K line feature to investigate a more detailed Fe K line flux asymmetry. We compare the Fe K emission feature in the combined spectrum from equally sized (radius ∼4″) northeast (NE), northwest (NW), southeast (SE), and southwest (SW) quadrant regions. We follow the same prescriptions described in Section 3.1 to perform a broadband spectral fit to measure the Fe abundance associated with the hard component, and a narrowband fit around the Fe K line (5.0–8.0 keV) to measure the emission line flux across the four quadrants.

In Figure 12, we present the flux distributions associated with Fe K emission across the four quadrants. We find that the strongest Fe K flux is observed in the NE quadrant. We also confirm that, on average, the total flux from the eastern half is stronger than the western half, as expected from analyzing the integrated spectrum from each epoch (Figure 11). The significant flux difference between the NE and SW quadrants could suggest that X-ray emission from the reverse shock is first emerging in the NE quadrant.

Recent NIRSpec JWST observations of SNR 1987A have revealed two primary Fe-rich plumes of ejecta, moving in the NE and SW directions (Larsson et al. 2023). Such a blueshifted NE plume and a redshifted SW plume geometry of the Fe ejecta were predicted by the MHD model described in Orlando et al. (2020). If the remnant interacts first with the ER in the eastern hemisphere, a reflected shock results earlier in the east than in the west, pushing the reverse shock in the eastern half to propagate through the innermost ejecta earlier than in the western side. This could potentially lead to the interaction of the reverse shock with the plume in the NE quadrant first, followed by the SW quadrant at a later time. The JWST NIRSpec images illustrate that the plume propagating to the NE lies in the plane of the ring, whereas the plume propagating to the SW does not (see Figure 4 in Larsson et al. 2023). Consequently, the majority of the material in the SW Fe-rich plume is situated farther away from the reverse shock. So, the possibility that the reverse shock is more internal in the eastern half than in the western half due to an earlier interaction with the ring, coupled with the fact that the NE plume is closer to the reverse shock (being planar with the ER) than the SW plume, makes it plausible that the interaction between Fe-rich ejecta and the reverse shock (radiating in X-rays) occurs first within the NE plume, consistent with our results (Figure 12).

Future Chandra observations of the strengthening Fe K line would be useful for constraining the potential blue- and redshifts among the observed Fe K line profiles in the NE and SW quadrants, respectively. If the Fe K feature is indeed strengthening with time after 2022, we expect better count statistics between ∼6 and 7 keV to be able to map out the spatial distribution of the Fe K line flux in comparison to that of the underlying continuum, for which Chandra data are uniquely suited. Testing for spatially differential developments of the reverse shock between the eastern and western sides of the SN and the robust measurements of enhanced Fe abundance with future high-resolution X-ray spectroscopy would also provide useful observational limits to constrain modeling of the explosion physics and the nature of the progenitor of SN 1987A.

4.3. Evolution of the Forward Shock

The overall radial expansion rate of SNR 1987A in the broadband images between 2016 and 2023 is approximately linear, similar to that between 2004 and 2016. This suggests that the peak X-ray emission from SNR 1987A is still dominated by the bright ER emission as of 2023. On the other hand, the width of the X-ray-emitting ring has increased to ∼0.″27 in 2022, whereas it stayed at ∼0.″20 until 2012. The width of the X-ray ring increased linearly from 2012 to 2022 at

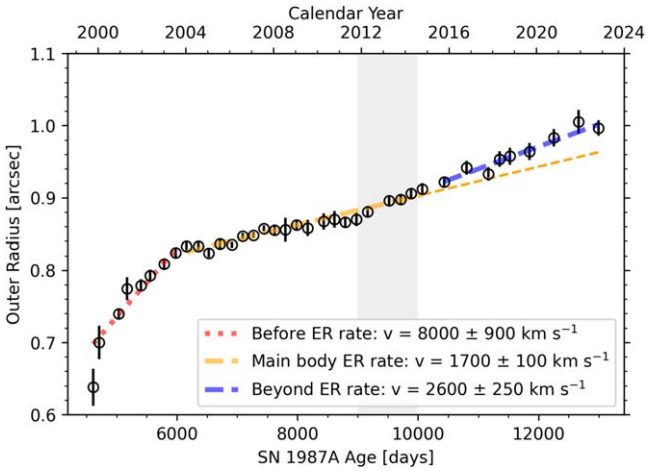

Figure 13. Evolution of the outer radius, $r_{\rm outer} = r_0 + \sigma_0/2$, where r_0 is the peak emission radius, and σ_0 is the best-fit width of the ring. We approximate the outer radius of SNR 1987A as the location of the blast wave. The best-fit linear expansion rates are overlaid for three epochs: before the shock enters the main body of the dense ER (red), during the shock interaction with the main body of the ER (yellow), and after the shock enters the low-density CSM beyond the main body of the ER (blue). The expansion rate during the shock interaction with the dense ER (orange dashed line) is extrapolated to compare with the expansion rate beyond the ER. The vertical shaded band (gray) between ∼2012 and 2016 marks the epochs when the size of the hardband X-ray SNR reached that of the softband and broadband SNR (as shown in Figure 8).

a rate of ∼4% per year. While the net increase of ∼0.″07 in the X-ray ring width from 2012 to 2022 is small and comparable with the ACIS astrometry limit, we note that our best-fit measurements of the ring width consistently show a systematic increase over a dozen epochs covering several years, while they were staying constant for the previous decade. Also, the measured width in 2022 (∼0.″27) is comparable to the effective spatial resolution of our ACIS images (see Section 3.2). Thus, we conclude that the recent increase in the ring width over the past decade is real. Based on these results, we trace the radius of the outer boundary of the X-ray remnant with $r_0 + \sigma_0/2$, where r_0 is the X-ray radius associated with the peak emission, and σ_0 is the width of the X-ray emitting ring in our image model fits (see Section 3.5).

In Figure 13, we plot the outer radius of SNR 1987A. The outer radius was expanding at a speed of 8000 ± 900 km s^{-1} until 2004, when the forward shock entered the main body of the ER. This high expansion rate is similar (within uncertainties) to that measured for the peak X-ray emission (Frank et al. 2016). It may indicate that before the forward shock hit the main body of the ER, the peak intensity and the outer boundary of the X-ray SNR 1987A were approximately comoving at similar velocities. Once the shock entered the main body of the ER, the expansion rate of the outer boundary of the SNR slowed down to 1700 ± 100 km s^{-1} while the shock interacted with the dense ER. This velocity is similar (within uncertainties) to the overall velocity of the peak emission during this period (Figure 8(a), Frank et al. 2016), which may indicate a strong deceleration of the shock front (outer boundary) as it entered the main body of the ER.

Sometime between 2012 and 2016, the outer edge started to expand faster (2600 ± 250 km s^{-1}—Figure 13), indicating that the shock was starting to move out of the ER. This epoch also coincides with the time period when the soft, hard, and broad energy band images all had similar best-fit radii, beyond which the hardband images started becoming larger than their broadband counterparts (Figure 8(b)). Before 2012 (day ∼9000), the hardband images were smaller, likely because of a significant contribution from the low-density H II region interior to the ER. Later (∼2012–2016), even in the hard band, ER (interclump regions) emission dominates, and hence all subband images have roughly the same size. After ∼2016, the hardband images became larger, as the increasing contribution of the spectrally hard X-ray emission from the shocked low-density CSM beyond the ER dominates the hardband X-ray emission. The blast wave starting to move out around ∼2012 (9000 days) is also consistent with our latest deep Chandra high-resolution gratings spectroscopic results, where a significant decline in the density profile of the shocked CSM was detected between days ∼8800 and ∼11,350 (Ravi et al. 2021). We note that while the origin of X-ray and radio emission may be different, a similar reacceleration of the shock wave in SNR 1987A was also reported in the radio band (Cendes et al. 2018).

4.4. Compact Remnant in SN 1987A

The presence of a pulsar wind nebula (PWN) was suggested in SNR 1987A, based on the NuSTAR observations, in which hard X-ray emission is detected at $E \sim 10$–20 keV (Greco et al. 2021, 2022). We note that the third hard spectral component (thermal or nonthermal) that was invoked to describe the NuSTAR spectrum of SNR 1987A (Alp et al. 2021; Greco et al. 2021) is not required to fit the observed X-ray spectrum of SNR 1987A in the Chandra bandpass. While the origin of this hard X-ray emission is debated (Alp et al. 2021), high-resolution ALMA data (Cigan et al. 2019) and recent IR spectra with JWST (Fransson et al. 2024) show evidence of the reprocessed emission due to photoionization of the surrounding cold ejecta from the neutron star, supporting the PWN interpretation.

We have not yet detected any emission from the central object in 0.3–8.0 keV Chandra images. This is not surprising, as recent estimates of the H column density due to the presence of cold ejecta toward the center of SNR 1987A are of order $\geqslant 10^{23}$ cm^{-2} (Esposito et al. 2018; Page et al. 2020; Greco et al. 2021). At such high column densities, the potential signatures of a compact object will be unlikely to be detected below 10 keV. In the future, as the central cool ejecta gas thins out and the absorption column density decreases, Chandra imaging will be crucial to directly identify the presence of the putative point source.

5. Conclusions

In this work, we report the results from our imaging-spectroscopic study of SNR 1987A based on 47 epochs of Chandra observation, spanning the last 23 yr. We reprocessed the entire data sets of our Chandra monitoring observations of SNR 1987A for a self-consistent analysis. Here we summarize our main results as below:

1. The soft X-ray light curve declines linearly between 2016 and 2020 (by ∼4.5% yr^{-1}), consistent with a physical picture where the forward shock is now propagating into the lower-density CSM outside the ER.
2. Since 2018, we detect for the first time in the Chandra spectrum the Fe K emission line feature at $E \sim 6.7$ keV. We find hints for the asymmetric distribution of the Fe K line flux between the eastern and western halves of the

SNR. This development could be either due to the strengthening of emission from an asymmetric distribution of CSM and/or the asymmetric reverse shock developing in SNR 1987A. Future Chandra observations will be crucial to discriminate between these origin scenarios.

3. The soft X-ray light curve since 2020 has stabilized once again at $\sim 7 \times 10^{-12}$ erg s^{-1} cm^{-2}. These observations, coupled with the presence of the Fe K line increasing in significance, could suggest the onset of contributions from the reverse-shocked ejecta. Comparisons with MHD simulations show that the evolution of the observed soft X-ray light curve is consistent with increasing contributions from reverse shock and outer ejecta interactions.
4. Since 2016, the peak emission radii measured in our Chandra images have expanded at a similar rate as before 2016 (1830 ± 40^{-1} km s^{-1}), suggesting that the dominant X-ray emission observed by Chandra is still within the ER. On the other hand, while the thickness of the X-ray emitting ring was constant between 2004 and 2016, it increased systematically (by $\sim$35%) between 2016 and 2022. This suggests that the outer boundary of the shock front in SNR 1987A is interacting with less-dense CSM beyond the dense ER. Also, the 3.0–8.0 keV hard images are increasing at a faster rate (2970 ± 150 km s^{-1}), growing larger than the broadband images as of 2022, which indicates a significant contribution of the spectrally hard X-ray emission from the shocked low-density CSM beyond the ER in the hardband X-ray image.

Acknowledgments

This paper employs a list of Chandra data sets obtained by the Chandra X-ray Observatory, contained in doi:10.25574/cdc.214.

We thank the anonymous referee for their careful and constructive consideration of our work. This work was supported in part by NASA Chandra grants G07-18060A, G08-19057X, G08-19043B, G09-20051B, and G02-23037X. S.O. and M.M. acknowledge financial contribution from the PRIN MUR "Life, death and after-death of massive stars: reconstructing the path from the presupernova evolution to the supernova remnant."

Facility: CXO (ACIS-HETG, HRC-S/LETG).

ORCID iDs

Aravind P. Ravi https://orcid.org/0000-0002-7352-7845
Sangwook Park https://orcid.org/0000-0003-3900-7739
Salvatore Orlando https://orcid.org/0000-0003-2836-540X
Marco Miceli https://orcid.org/0000-0003-0876-8391
Kari A. Frank https://orcid.org/0000-0003-0570-9951
Patrick S. Broos https://orcid.org/0000-0002-7872-2025
David N. Burrows https://orcid.org/0000-0003-0729-1632

References

Alp, D., Larsson, J., & Fransson, C. 2021, ApJ, 916, 76
Arendt, R. G., Dwek, E., Bouchet, P., et al. 2016, AJ, 151, 62
Arendt, R. G., Dwek, E., Bouchet, P., et al. 2020, ApJ, 890, 2
Arnaud, K. A. 1996, in ASP Conf. Ser. 101, Astronomical Data Analysis Software and Systems V, ed. G. H. Jacoby & J. Barnes (San Francisco, CA: ASP), 17
Arnett, W. D., Bahcall, J. N., Kirshner, R. P., & Woosley, S. E. 1989, ARA&A, 27, 629
Asplund, M., Grevesse, N., Sauval, A. J., & Scott, P. 2009, ARA&A, 47, 481
Borkowski, K. J., Blondin, J. M., & McCray, R. 1997, ApJL, 476, L31
Borkowski, K. J., Lyerly, W. J., & Reynolds, S. P. 2001, ApJ, 548, 820
Bray, E., Burrows, D. N., Park, S., & Ravi, A. P. 2020, ApJ, 899, 21
Broos, P. S., Townsley, L. K., Feigelson, E. D., et al. 2010, ApJ, 714, 1582
Burrows, C. J., Krist, J., Hester, J. J., et al. 1995, ApJ, 452, 680
Burrows, D. N., Michael, E., Hwang, U., et al. 2000, ApJL, 543, L149
Carter, C., Karovska, M., Jerius, D., Glotfelty, K., & Beikman, S. 2003, in ASP Conf Ser. 295, Astronomical Data Analysis Software and Systems XII, ed. H. E. Payne, R. I. Jedrzejewski, & R. N. Hook (San Francisco, CA: ASP), 477
Cendes, Y., Gaensler, B. M., Ng, C. Y., et al. 2018, ApJ, 867, 65
Chevalier, R. A., & Dwarkadas, V. V. 1995, ApJL, 452, L45
Cigan, P., Matsuura, M., Gomez, H. L., et al. 2019, ApJ, 886, 51
Dewey, D., Dwarkadas, V. V., Haberl, F., Sturm, R., & Canizares, C. R. 2012, ApJ, 752, 103
Dewey, D., Zhekov, S. A., McCray, R., & Canizares, C. R. 2008, ApJL, 676, L131
Esposito, P., Rea, N., Lazzati, D., et al. 2018, ApJ, 857, 58
Frank, K. A., Zhekov, S. A., Park, S., et al. 2016, ApJ, 829, 40
Fransson, C., Barlow, M. J., Kavanagh, P. J., et al. 2024, Sci, 383, 898
Fransson, C., Larsson, J., Migotto, K., et al. 2015, ApJL, 806, L19
Fransson, C., Lundqvist, P., & Chevalier, R. A. 1996, ApJ, 461, 993
Greco, E., Miceli, M., Orlando, S., et al. 2021, ApJL, 908, L45
Greco, E., Miceli, M., Orlando, S., et al. 2022, ApJ, 931, 132
Haberl, F., Geppert, U., Aschenbach, B., & Hasinger, G. 2006, A&A, 460, 811
Helder, E. A., Broos, P. S., Dewey, D., et al. 2013, ApJ, 764, 11
Kallman, T. R., Palmeri, P., Bautista, M. A., Mendoza, C., & Krolik, J. H. 2004, ApJS, 155, 675
Larsson, J., Fransson, C., Alp, D., et al. 2019, ApJ, 886, 147
Larsson, J., Fransson, C., Sargent, B., et al. 2023, ApJL, 949, L27
Larsson, J., Fransson, C., Spyromilio, J., et al. 2016, ApJ, 833, 147
Lucy, L. B. 1974, AJ, 79, 745
Luo, D., & McCray, R. 1991, ApJ, 379, 659
Maggi, P., Haberl, F., Sturm, R., & Dewey, D. 2012, A&A, 548, L3
Makishima, K. 1986, in The Physics of Accretion onto Compact Objects, ed. K. O. Mason, M. G. Watson, & N. E. White (Berlin: Springer-Verlag), 249
Mattila, S., Lundqvist, P., Gröningsson, P., et al. 2010, ApJ, 717, 1140
McCray, R. 1993, ARA&A, 31, 175
McCray, R., & Fransson, C. 2016, ARA&A, 54, 19
Mori, K., Tsunemi, H., Miyata, E., et al. 2001, in ASP Conf. Ser. 251, New Century of X-ray Astronomy, ed. H. Inoue & H. Kunieda (San Francisco, CA: ASP), 576
Morris, T., & Podsiadlowski, P. 2007, Sci, 315, 1103
Ng, C. Y., Zanardo, G., Potter, T. M., et al. 2013, ApJ, 777, 131
O'Dell, S. L., Swartz, D. A., Tice, N. W., et al. 2013, Proc. SPIE, 8859, 88590F
Ono, M., Nagataki, S., Ferrand, G., et al. 2020, ApJ, 888, 111
Orlando, S., Miceli, M., Petruk, O., et al. 2019, A&A, 622, A73
Orlando, S., Miceli, M., Pumo, M. L., & Bocchino, F. 2015, ApJ, 810, 168
Orlando, S., Ono, M., Nagataki, S., et al. 2020, A&A, 636, A22
Page, D., Beznogov, M. V., Garibay, I., et al. 2020, ApJ, 898, 125
Park, S., Burrows, D. N., Garmire, G. P., et al. 2002, ApJ, 567, 314
Park, S., Zhekov, S. A., Burrows, D. N., Garmire, G. P., & McCray, R. 2004, ApJ, 610, 275
Park, S., Zhekov, S. A., Burrows, D. N., & McCray, R. 2005, ApJL, 634, L73
Park, S., Zhekov, S. A., Burrows, D. N., et al. 2006, ApJ, 646, 1001
Park, S., Zhekov, S. A., Burrows, D. N., et al. 2011, ApJL, 733, L35
Plucinsky, P. P., Bogdan, A., Marshall, H. L., & Tice, N. W. 2018, Proc. SPIE, 10699, 106996B
Potter, T. M., Staveley-Smith, L., Reville, B., et al. 2014, ApJ, 794, 174
Racusin, J. L., Park, S., Zhekov, S., et al. 2009, ApJ, 703, 1752
Ravi, A. P., Park, S., Zhekov, S. A., et al. 2021, ApJ, 922, 140
Richardson, W. H. 1972, JOSA, 62, 55
Romaniello, M., Riess, A., Mancino, S., et al. 2022, A&A, 658, A29
Russell, S. C., & Dopita, M. A. 1992, ApJ, 384, 508
Sturm, R., Haberl, F., Aschenbach, B., & Hasinger, G. 2010, A&A, 515, A5
Sugerman, B. E. K., Lawrence, S. S., Crotts, A. P. S., Bouchet, P., & Heathcote, S. R. 2002, ApJ, 572, 209
Sun, L., Vink, J., Chen, Y., et al. 2021, ApJ, 916, 41
Urbaneja, M. A., Kudritzki, R. P., Gieren, W., et al. 2017, AJ, 154, 102
Wang, L., & Mazzali, P. A. 1992, Natur, 355, 58
Zanardo, G., Staveley-Smith, L., Indebetouw, R., et al. 2014, ApJ, 796, 82
Zhekov, S. A., McCray, R., Borkowski, K. J., Burrows, D. N., & Park, S. 2006, ApJ, 645, 293
Zhekov, S. A., McCray, R., Dewey, D., et al. 2009, ApJ, 692, 1190
Zhekov, S. A., Park, S., McCray, R., Racusin, J. L., & Burrows, D. N. 2010, MNRAS, 407, 1157